CrossMark

REGULAR PAPER

J. M. Yu · T. S. Leu · J. J. Miau

Investigation of reduced frequency and freestream turbulence effects on dynamic stall of a pitching airfoil

Abstract In this study, the dynamic stall evolutions were investigated using particle image velocimetry (PIV) in a water channel with Reynolds number $Re = 4.5 \times 10^3$ based on the chord length. The airfoil pitching waveform was performed under the condition calculated from the angle of attack histogram of a vertical axis wind turbine (VAWT). Using PIV, the instantaneous vorticity contours and streamlines can be revealed. Based on the formation of the leading edge vortex, the stall angle can be explored at reduced frequency $k = 0.09$, 0.18, and 0.27. It was found that the stall angle was delayed from the angle of attack $\alpha = 16°$ to $\alpha = 30°$ as reduced frequency increased from $k = 0.09$ to 0.27. The hysteresis effect of stall angle delay was more pronounced for high reduced frequency. Moreover, the freestream turbulence effect on the pitching airfoil was investigated with turbulence intensity TI = 0.5 and 6.9 %. As found, the stall angles were postponed to higher angles of attack for the high turbulence intensity. The phase difference between TI = 0.5 and 6.9 % were $\Delta\alpha = 8°$, 4°, and 4° for $k = 0.09$, 0.18, and 0.27, respectively. For TI = 6.9 %, enhanced turbulence mixing reduces the velocity deficit ($u/U < 1$) and flow reversal ($u/U < 0$). In addition, the maximum velocity is reduced from $u/U = 1.8$ to 1.2 and the S-shaped velocity profile is diminished or weakened for TI = 6.9 %. Thus, the dynamic stall is further delayed to the downstroke. The circulation values increase rapidly to maximum and then drop quickly after dynamic stall for $k = 0.18$ and 0.27.

Keywords Dynamic stall · Pitching airfoil · Reduced frequency effect · Freestream turbulence

1 Introduction

Strong growth of utilizing wind energy in the past decade stimulates extensive research efforts on the wind turbine technology nowadays. Recently, a great attention has been paid to investigate the aerodynamic performance of vertical axis wind turbines (VAWT) due to their potential applications in urban environments; for instance, the idea of installing a small wind turbine on the roof of a building was explored (Fujisawa and Takeuchi 1999; Islam et al. 2008). However, VAWT faces a critical challenge, especially operating at a low tip speed ratio (Ameku et al. 2008; Chen and Kuo 2012). The angle of attack of the blades will exceed the static stall angle at low tip speed ratio leading to the aerodynamics of VAWT which involves highly unsteady flow fields. Dynamic stall is an inherent phenomenon at the low tip speed ratio impacting on power, loads, and fatigue of the blades (Chen et al. 2010; Jin et al. 2014; Ubaldi and Zunino 2000). Therefore, the unsteady aerodynamic behavior and the phenomenon of dynamic stall of VAWT blades represent a challenging subject to be investigated.

J. M. Yu · T. S. Leu (✉) · J. J. Miau
Department of Aeronautics and Astronautics, National Cheng Kung University, Tainan 70101, Taiwan
E-mail: tsleu@mail.ncku.edu.tw

Dynamic stall phenomena have attracted a number of studies for years with a wide range of practical applications such as wind turbines, manmade and natural flyers, and marine energy convertors (Karbasian et al. 2016b). These phenomena are associated with pitch/plunge oscillating and flapping airfoils have been simulated above practical applications. For instance, Rival et al. (2008) used the particle image velocimetry (PIV) to investigate the formation process of leading edge vortices in bio-inspired flight. The similar kinematics of flying of birds and swimming of the penguins can be observed by evaluating the elliptical motion tractor on the aerodynamic characteristics and propulsive performance of a flapping airfoil (Esfahani et al. 2015). In other words, the complex dynamic stall phenomena can be employed in a simplified configuration of pitch/plunge oscillating and flapping airfoils to study its main characteristics (Bousman 2001; McCroskey 1982; Yen and Ahmed 2013). Dynamic stall can be considered as delay of flow separation on wings and airfoils caused by rapid variations in the angle of attack beyond the critical static stall angle (Carr 1988). The conditions of dynamic stall can be divided into four distinct regimes which are under stall, stall onset, light stall and deep stall, respectively (McCroskey 1982). In the deep stall regime particularly, pitching amplitude well in excess of the static stall angle begins with the formation of a strong vortex in the leading edge. This strong vortex is so-called core vortex which is sensitive to the unsteady parameters such as reduced frequency, pitching angle and freestream turbulence intensity (Corke and Thomas 2014). Digavalli (1994) reported that upstream movement of the separation point and the inception of the primary vortex are delayed for reduced frequency $k = 0.6$–1.2.

In the practical situation, VAWT often operates inside an atmospheric turbulent boundary layer. The most available data of pitching airfoil were under the uniform freestream and low turbulence intensity condition, which is not completely representative of the actually operated condition. Therefore, to meet the particular operated condition of VAWT, unsteady freestream velocity and freestream with high turbulence intensity acting on the airfoil to capture the effect of freestream characteristics on the dynamic stall should be taken into account. Gharali and Johnson (2015) investigated the effect of unsteady incident velocity on a pitching S809 airfoil in Reynolds number of 10^6 using 2D numerical simulation. The result presented that strong dependency on the velocity and acceleration of the freestream during the dynamic stall. Karbasian et al. (2016a) further indicated that the lift is influenced significantly by the airfoil acceleration motion. However, the drag for different airfoil acceleration motion is approximately identical.

The purpose of this study is to investigate the reduced frequency and freestream turbulence effects on the dynamic stall. The digital particle image velocimetry (PIV) technique was employed in the water channel to explore the variation of vorticity field, streamlines and circulation with the specific angle of attacks. Particular attention is given to the variation of dynamic stall phenomena and associated vortex structures in the presence of freestream turbulence intensity. By investigating the dynamic stall in the pitching airfoil experiments, one can have more insights what would occur for VAWT.

2 The pitching motion

The airfoil pitching waveforms in the present experiments were calculated from the angle of attack histogram of a vertical axis wind turbine (VAWT) at different tip speed ratios (λ). For the cases of the tip speed ratio of $\lambda = 2$, pitching amplitudes of the waveforms are $\alpha = 30°$ for three different reduced frequencies as shown in Fig. 1. The relation between the incidence angle (α) of the flow and the tip speed ratio (λ) of VAWT can be described as follows (Islam et al. 2008):

$$\alpha = \tan^{-1}\left(\frac{\sin(2\pi ft)}{\lambda + \cos(2\pi ft)}\right) \tag{1}$$

where α = the angle of attack of the airfoil, f = pitching frequency (Hz).

Amet et al. (2009) presented that power curve of VAWT was affected by dynamic stall, especially at low tip speed ratio. In this study, a maximum angle of attack of $\alpha = 30°$ corresponds to $\lambda = 2$ was conducted. According to the Eq. (1), the conducted angles of attack are associated with low tip speed ratios. In other words, the aims of this study were to simulate variation of the angle of attack of VAWT in the influence of dynamic stall regions by performing a variety of pitching rates. Furthermore, one of the significant parameters in describing the level of unsteady of pitching motion was reduced frequency. It presents the ratio of convective time scale (C/U_∞) and the time scale of the forced oscillation ($1/\pi f$) (Leishman 2006). The mathematic expression can be presented as follows:
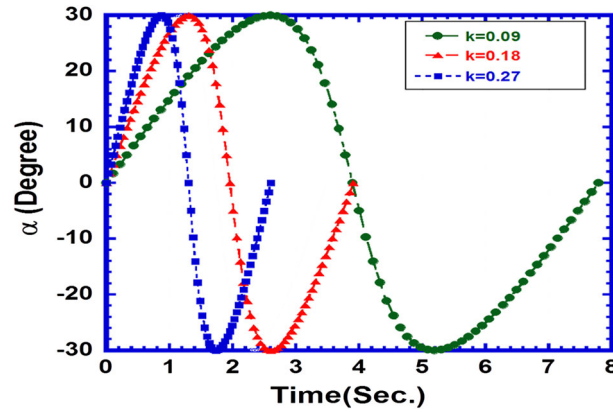
Fig. 1 The waveform of pitching airfoil

$$k = \frac{\pi f C}{U_\infty} \tag{2}$$

where, f = pitching frequency (Hz), C = chord length of pitching airfoil.

In the present study, three reduced frequencies were considered to investigate the effect of reduced frequency, where $k = 0.09$, 0.18, and 0.27 as shown in Fig. 1. Leishman (2006) investigated the effect of the reduced frequency on unsteady aerodynamic of pitching blades. For $0 < k < 0.05$, the flow unsteady effect was generally small and the flow can be considered quasi-steady. For $k \geq 0.05$, the flow was defined unsteady.

3 Experimental setup

A closed-loop water channel with a rectangular test section of a height of 600 mm and a width of 600 mm was employed. The bottom and side walls of test section were made of acrylic for the purpose of visualization. To reduce the turbulent intensity and provide uniformed flow distribution, honeycomb, and stainless screen were installed in the settling chamber. The flow was pumped by a DC inverter motor. The maximum freestream velocity reaches to 0.4 m/s and the streamwiseturbulence intensity (TI) in the measured range was less than 0.5 %. For the purpose of investigating the turbulence effect on the pitching airfoil, a turbulence generator has been installed in the inlet of the test section. Grids are the classical type to generate turbulence and its turbulence intensity delays with the distance (Taylor 1935). The turbulence generator was constructed with a wooden square bar mesh. The cross section of wooden square bars (d) was 10 mm by 10 mm with a mesh size (M) of 30 mm. The distance between the turbulence generator and the location of turbulence intensity measurement was 285 mm to ensure the homogeneous turbulence was reached. The measured freestream turbulence intensity (TI) at the location of test airfoil section was equal to 6.9 %. The porosity, β, is the most important parameter with respect to the screen geometry. The β is presented as $\beta = (1 - d/M)^2$. To avoid the jets emanating which lead to large-scale mean velocity variation from the hole of screen, Kurian and Fransson (2009) have suggested the porosity should be larger than about $\beta \geq 0.55$. In the present configuration, the $\beta = 0.55$ which meets the suggestion value. Figure 2 shows the apparatus with the turbulence generator for the experiments.

The airfoil, NACA 0015, of the chord length $C = 30$ mm and the aspect ratio AR = 5, was pivoted at $x = 0.3C$, which was a non-dimensional pitch axis of location from the leading edge. In addition, the airfoil profile was used in our previous VAWT models for investigating the power and torque coefficients (Chen et al. 2010; Miau et al. 2012). The airfoil was made of transparent acrylic for PIV measurement. The surfaces were painted as black color except the middle area of the airfoil which allows the laser light sheet to pass through to illuminate the tracing particles. This method enhanced visual contrast and reduced the laser reflection during the experiment. The airfoils were driven by the servo motor with a driving mechanism capable of controlling the pitching rate of the airfoil model with a predefined waveform. The airfoil model was installed between two blackening end plates. The gap between the model and either of end plates was about 1 mm to eliminate the tip vortex. As a result, the flow could be considered two dimensional.
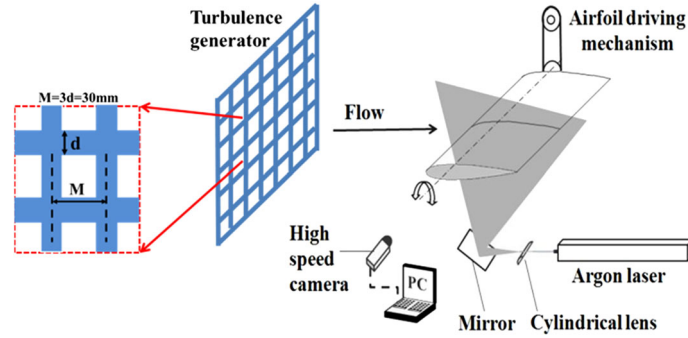
Fig. 2 Schematic sketch of the experimental setup

All the experiments were conducted at freestream velocity $U_\infty = 13.37$ cm/s, which corresponds to Reynolds number Re $(U\infty C/\upsilon) = 4.5 \times 10^3$. The phenomenon of the dynamic stall was investigated using particle image velocimetry (PIV) techniques. As shown in Fig. 2, a typical PIV measurement system was consisting of a laser source for illuminating the seeding particles, seeding particle with proper density and size for tracing flow, optical lenses for generating laser light sheet, high-speed camera to capture the image and post-processing software to compute the experimental data. The illumination was made by laser light sheet to visualize the two-dimensional flow phenomena in the vertical plane of the test section. The laser used in the present study was a continuing argon laser with a maximum energy of 5 W (Innova 70, Coherent) and wavelength 488 nm. The thickness of the laser sheet is about 1 mm. The hollow silicon dioxide microspheres with 10 μm diameter and specific gravity of 1.0 g/cm³ were used as tracer particles (10089, TSI). The observation was made by a monochrome high-speed digital CMOS camera (Photron FASTCAM SA-X) having image size and resolution of 1280 pixel × 1024 pixel with 12 bits. The frame rate of the camera was 500 frame/s which allowed for the sequential imaging at a time interval of 2 μs. The digital image sequences are analyzed with commercial software (PIV View) to obtain the velocity vector and vorticity distributions. The observation area of the high-speed camera was 110 mm by 110 mm so that the whole flow field around the airfoil during the pitching motion could be imaged. The spatial resolution of the captured images was about 9.3 pixel/mm. The instantaneous vorticity contours and streamlines were obtained by analyzing two sequential images with cross-correlation calculation. The interrogation window was set as 24 by 24 pixels and that overlapped region was 50 % to satisfy the Nyquist sampling criterion.

To compare the LEV strengths, the dimensionless circulation was calculated from the vorticity field via the integral method. Based on the Stoke's theorem, the circulation of a rectangular area A can be presented as:

$$\Gamma = \iint_A \omega_z \mathrm{d}A \tag{3}$$

where ω_z = spanwise vorticity (1/s), A = vortices integral area (mm²).

For the sake of comparing the clockwise vortex strength which is on the upper surface of the airfoil, the dimensionless vorticity, $\omega_z C/U_\infty$, and circulation, Γ/CU_∞, will be used later. The integral area was from $x/C = -0.3$ to 0.7 in x-direction and $y/C = -0.5$ to 0.5 in y-direction. The selected area can encompass the vorticity above the upper surface of the airfoil.

4 Results and discussion

To depict the typical phenomena of flow field under the dynamic stall, the vorticity contours superimposed with the streamlines are presented. The magnitude of vorticity is often used to express the strength of rotation of the fluid. Note that, the negative value of vorticity presents the clockwise rotation and the positive one is the counter-clockwise rotation. To investigate the reduced frequency and freestream turbulence effects on the dynamic stall, the investigations were performed when the leading edge vortex (LEV) arrives at the trailing edge. As the LEV propagates behind the trailing edge, the flow is fully separated and stall occurs. In the following, the experimental results are presented for $Re = 4.5 \times 10^3$, based on the chord length and freestream velocity. The low turbulence intensity (TI) of 0.5 % is used to investigate the reduced frequency effect, but the high one of 6.9 % is applied to observe the turbulence effect.
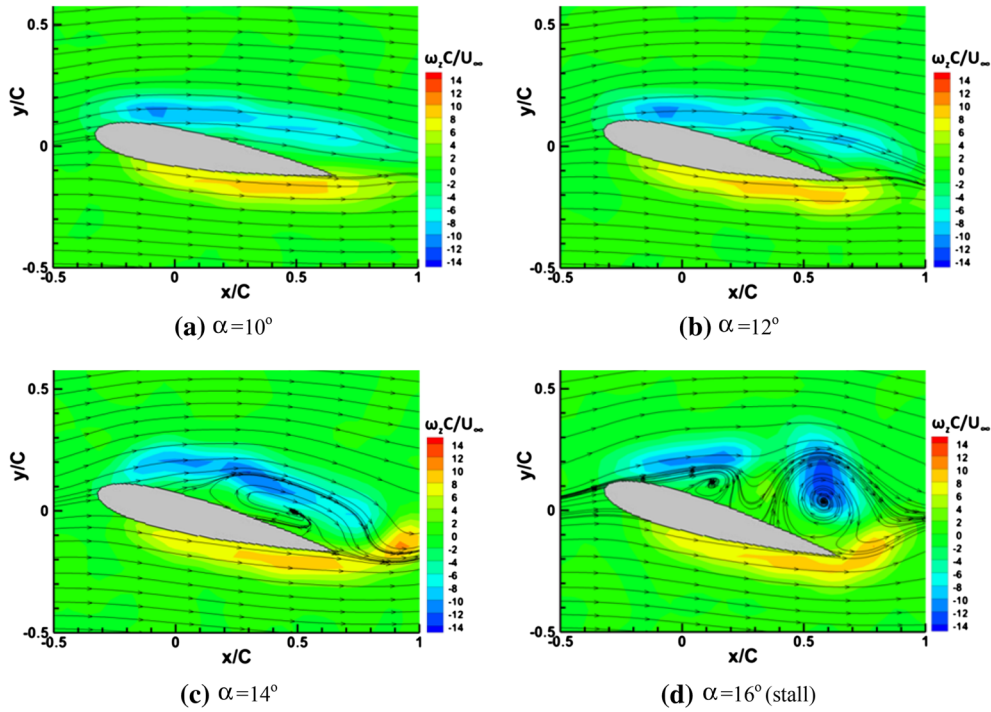
(a) α=10°

(b) α=12°

(c) α=14°

(d) α=16° (stall)

Fig. 3 Instantaneous vorticity field with streamlines at $k = 0.09$ (TI = 0.5 %; $Re = 4.5 \times 10^3$)

4.1 Reduced frequency effect (TI = 0.5 %)

Figure 3 shows the instantaneous dimensionless vorticity distribution with streamlines around the airfoil at a reduced frequency $k = 0.09$. When the angles of attack increase from $\alpha = 0°$ to $\alpha = 10°$, the flow is characterized by the laminar boundary layer which evolves slowly as shown in Fig. 3a. At these lower incidence angles, the vorticity values above the airfoil are very small and no obvious vortex can be observed. As seen from the vorticity distribution and streamlines at $\alpha = 12°$, the thickening of the vertical region in the mid-to-aft region of the airfoil is due to the presence of a small region of reverse flow near the trailing edge as shown in Fig. 3b. The reversed flow near the leading edge leads to the formation of the clockwise leading edge vortex (LEV) and growth in size as the angle of attack increases to $\alpha = 14°$ as shown in Fig. 3c. At $\alpha = 16°$, the secondary LEV forms and the first LEV propagates to the trailing edge. The LEV above the trailing edge induces the counter-clockwise fluid rotation behind the trailing edge as shown in Fig. 3d. The lift stall takes place while the first LEV arrives at the trailing edge (Leishman 2002). Note that the discrepancy between the maximum vorticity and vortex core may be attributed to the convection of the vortices with regard to the surrounding fluid (Hansen 2012).

For $k = 0.18$ at $\alpha = 16°$, the flow remains attached on the upper surface because the momentum addition by the pitching-up leading edge to flow. The added momentum is more prominent than the adverse pressure gradient. The vorticity above the airfoil is very small and the streamline is nearly parallel to the airfoil surface as shown in Fig. 4a. As compared to Fig. 3d for $k = 0.09$ at $\alpha = 16°$, the LEV is not yet obvious due to the hysteresis effect. At $\alpha = 22°$, a clockwise vortex, known as LEV, forms above the upper surface as shown in Fig. 4b. The LEV plays a significant role for the dynamic stall. The low pressure area of the LEV supplies the additional lift above the steady stall value and delays the stall angle (Tseng and Cheng 2015). Figure 4c shows that the LEV grows and a strong counter-clockwise vortex exists behind the trailing edge at $\alpha = 24°$. At $\alpha = 26°$, the LEV grows up continuously and covets the whole upper surface as shown in Fig. 4d. In the meantime, the lift reaches the maximum value when the LEV arrives at the trailing edge.

For the higher reduced frequency case, $k = 0.27$, the flow evolves slowly and remains attached to the airfoil when the angles of attack are below 24°. Thus, the flow can be sustained to deep stall angle without apparent vortex taking place above the upper surface. Further increasing the angle of attack to 24°, a small LEV appears near the leading edge as shown in Fig. 5a. The LEV grows bigger and becomes stronger with increasing angles of attack from 26° to 30° (Fig. 5b–d). At $\alpha = 30°$, the dynamic stall occurs when the LEV

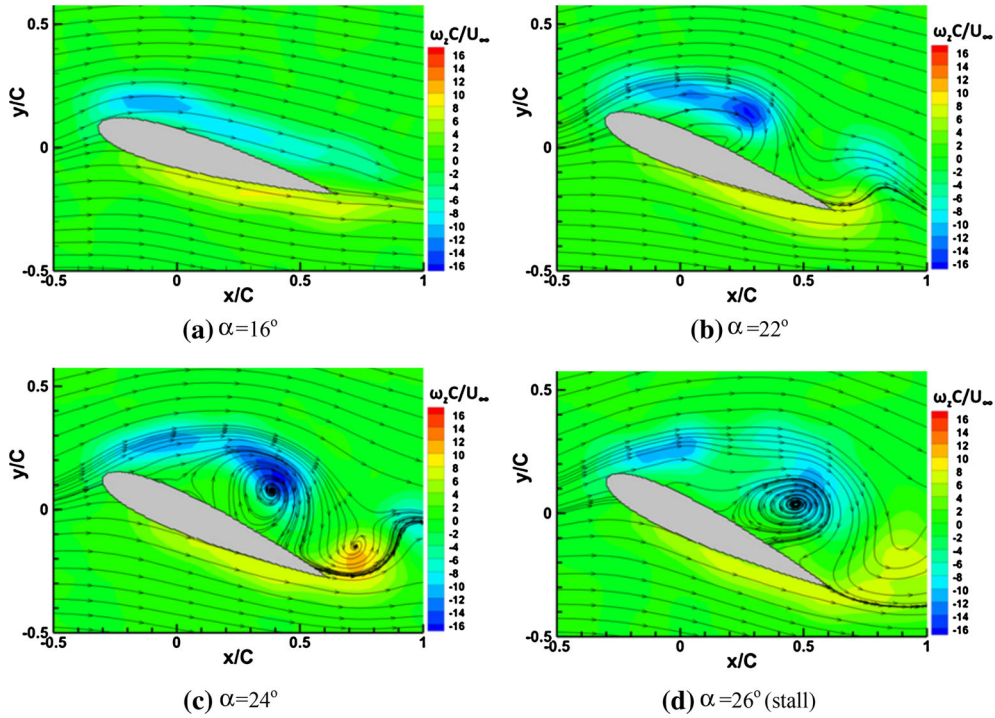**Fig. 4** Instantaneous vorticity field with streamlines at $k = 0.18$ (TI $= 0.5$ %; $Re = 4.5 \times 10^3$)
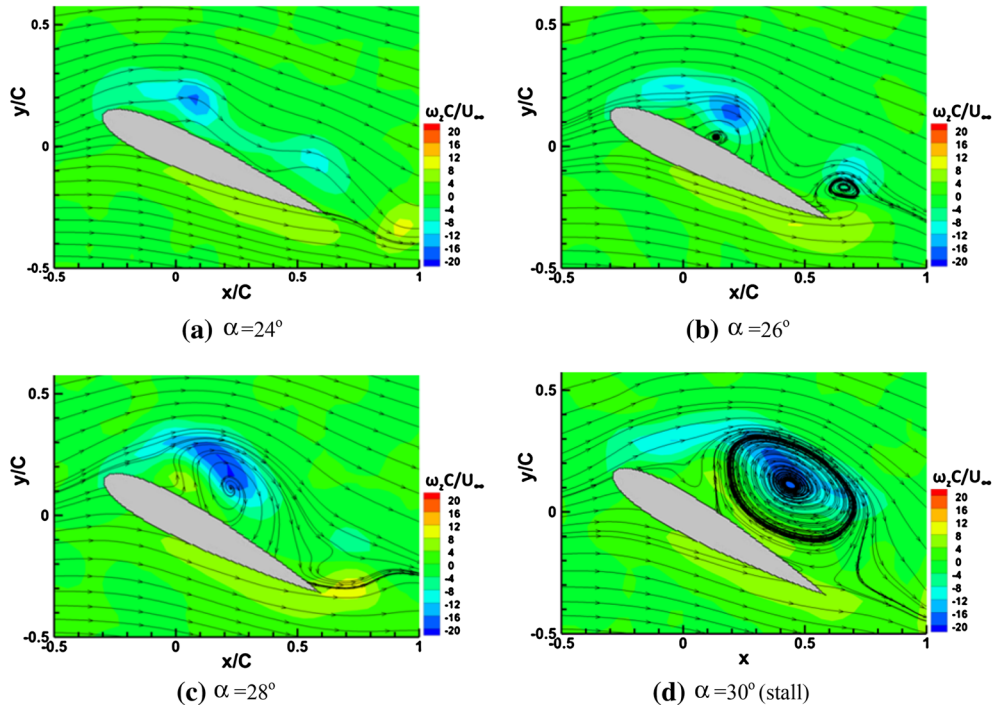

Fig. 5 Instantaneous vorticity field with streamlines at $k = 0.27$ (TI $= 0.5$ %; $Re = 4.5 \times 10^3$)

reaches the trailing edge. One feature of the higher reduced frequency effect on the dynamic stall is the delay of the dynamic stall to angles beyond the lower reduced frequency. As compared to Fig. 4d for $k = 0.18$ at $\alpha = 26°$, the LEV is much smaller for $k = 0.27$ at $\alpha = 26°$ as shown in Fig. 5b. This phase
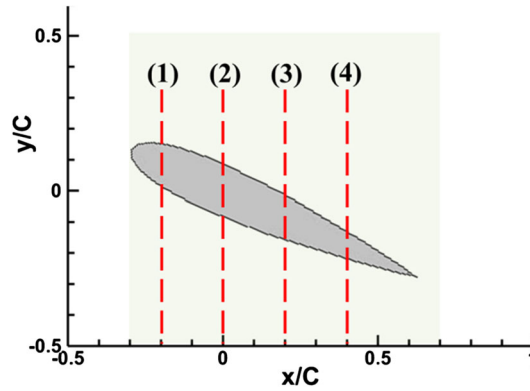
Fig. 6 The location of sampled velocity profile and integral area of circulation

delay is due to the combination of viscous diffusion time for the formation of the LEV and the convection time ($\approx C/U_\infty$) for the LEV to travel to the trailing edge.

By considering the reduced frequency effect with TI = 0.5 %, the stream wise velocity profiles were sampled along the vertical direction above the upper surface. The locations of the sampled velocity profiles are illustrated in Fig. 6. Note that the rectangular shaded area is used for the calculation of circulation in the later section. Comparing the ratio of local velocity and freestream velocity, the flow acceleration and deceleration can be observed during the dynamic stall. As the local velocity is less than the free stream velocity, the velocity deficit is investigated.

Figure 7 shows the velocity profiles at different stall angles of attack of $\alpha = 16°$, $\alpha = 26°$, and $\alpha = 30°$ for $k = 0.09$, 0.18, and 0.27, respectively. At $\alpha = 16°$, the acceleration is stronger near the leading edge as shown in Fig. 7a of cross section (1). The flow then decelerates to cross sections (2), (3), and (4). In Fig. 7a of cross section (3), the velocity deficit ($u/U \le 1$) for $k = 0.09$ is apparent due to the recirculation area above the suction surface where the LEV occupies as shown in Fig. 3d. For $k = 0.18$, the velocity profile appears to describe the laminar boundary layer, which is characterized by low vorticity values and smooth streamlines as shown in Fig. 4a. The velocity profiles for $k = 0.18$ and 0.27 are similar.

At $\alpha = 26°$, the shear layer grows from the leading edge (cross section 1) to the mid-chord regions (cross sections 2 and 3), and finally near the trailing edge (cross section 4) for $k = 0.18$ as shown in Fig. 7b. The flow continues to accelerate downstream until it reaches a maximum value about twice of the freestream velocity at $y/C = 0.38$ at the cross section (4). Conceivably, the full stall takes place due to the strong LEV near the trailing edge. This investigation is in agreement with the result by Tseng and Cheng (2015). The velocity near the wall surface turns to negative, indicating that the flow is reversed. The S-shaped velocity profile at the cross section (4) can be observed in Fig. 3d where the LEV exists.

Further increasing the angle of attack to $\alpha = 30°$, the reversed flow can be observed near the wall surface at cross section (4) for $k = 0.27$ as shown in Fig. 7c. The streamwise negative velocity near the wall surface for $k = 0.27$ is higher than that for $k = 0.09$ because more momentum can be transferred into the recirculation area. The flow with higher reduced frequency leads to more organized vortex structure, which is associated with stronger flow acceleration induced by the higher rotational velocity of the airfoil. The stronger acceleration leads to the maximum value to approximately twice the freestream velocity at $y/C = 0.38$ of cross section (4). This S-shaped velocity is similar to $k = 0.18$ at $\alpha = 26°$ in Fig. 7b at the same cross section location but the reversed flow is more pronounced in Fig. 7c for $k = 0.27$ and $\alpha = 30°$.

4.2 Turbulence effect

Regarding the flow fields with TI = 6. 9 %, the evolutionary process of dynamic stall is similar to that of TI = 0.5 %. For $k = 0.09$ at $\alpha = 16°$, the flow keeps attached on the upper surface as shown in Fig. 8a. However, for $k = 0.09$ at the same angle of attack $\alpha = 16°$ with TI = 0.5 %, the LEV can be observed clearly as shown in Fig. 3d. It indicates the significant feature of the turbulence effect which is the delay of the dynamic stall to an angle beyond the case with TI = 0.5 %. At angles of attack below $\alpha = 18°$, the flow is characterized by the laminar boundary layer and no obvious flow separation is present as shown in Fig. 8a, b. At $\alpha = 22°$, a clockwise LEV appears clearly above the upper surface as shown in Fig. 8c. The

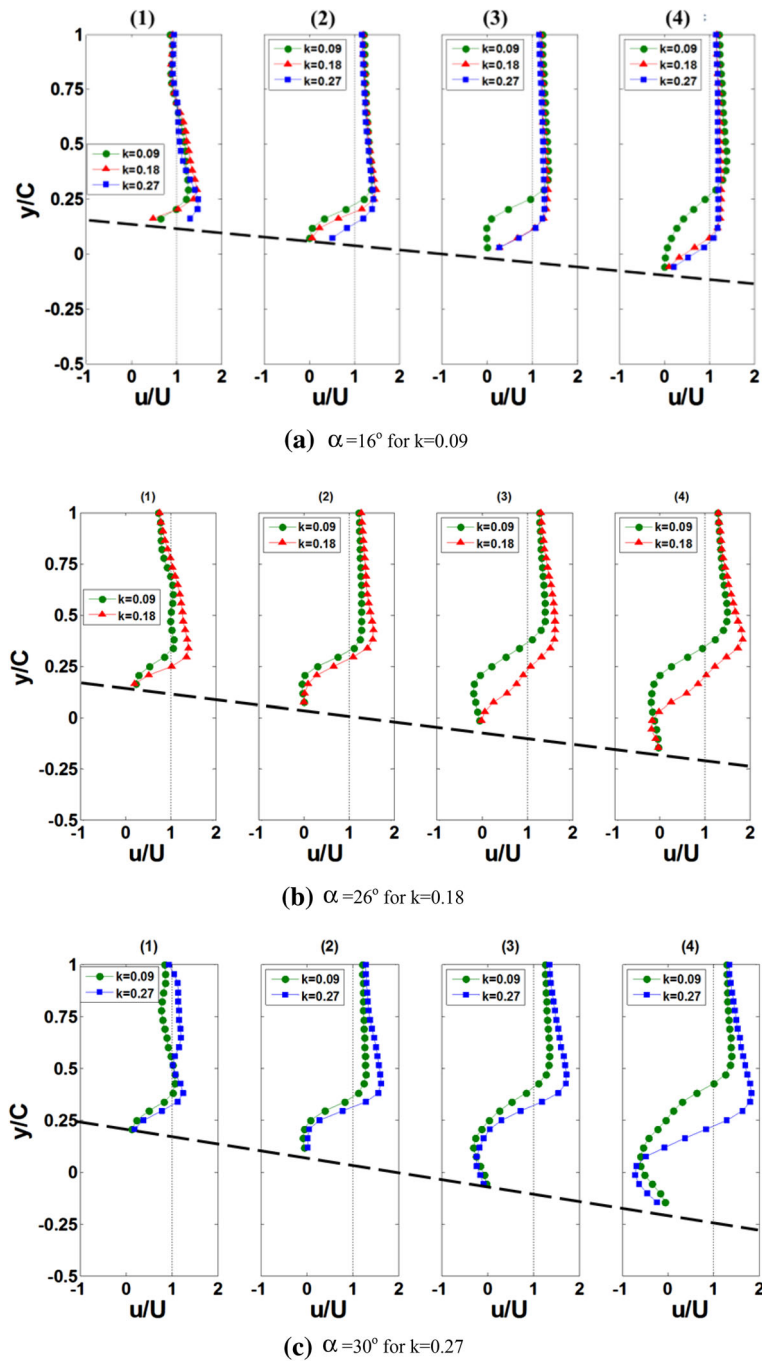**(a)** α =16° for k=0.09

(b) α =26° for k=0.18

(c) α =30° for k=0.27

Fig. 7 The dimensionless velocity profile for TI = 0.5 % (*black dashed line* is wall surface of the airfoil)

LEV grows in size and becomes an organized dynamic stall vortex from α = 22° to α = 24°. At α = 24° shown in Fig. 8d, the downstream boundary of LEV arrives at the trailing edge which leads to dynamic stall.

For k = 0.18 at α = 24°, a small vortex appears above the upper surface of mid-chord but is not obvious as shown in Fig. 9a. The boundary layer grows and LEV takes place near the leading edge at α = 26° as shown in Fig. 9b. Comparing the flow field at the same angle of attack α = 26°, instead of existing a large LEV above the upper surface for flow with TI = 0.5 % as shown in Fig. 4d, the LEV in Fig. 9b is smaller for flow with TI = 6.9 %.
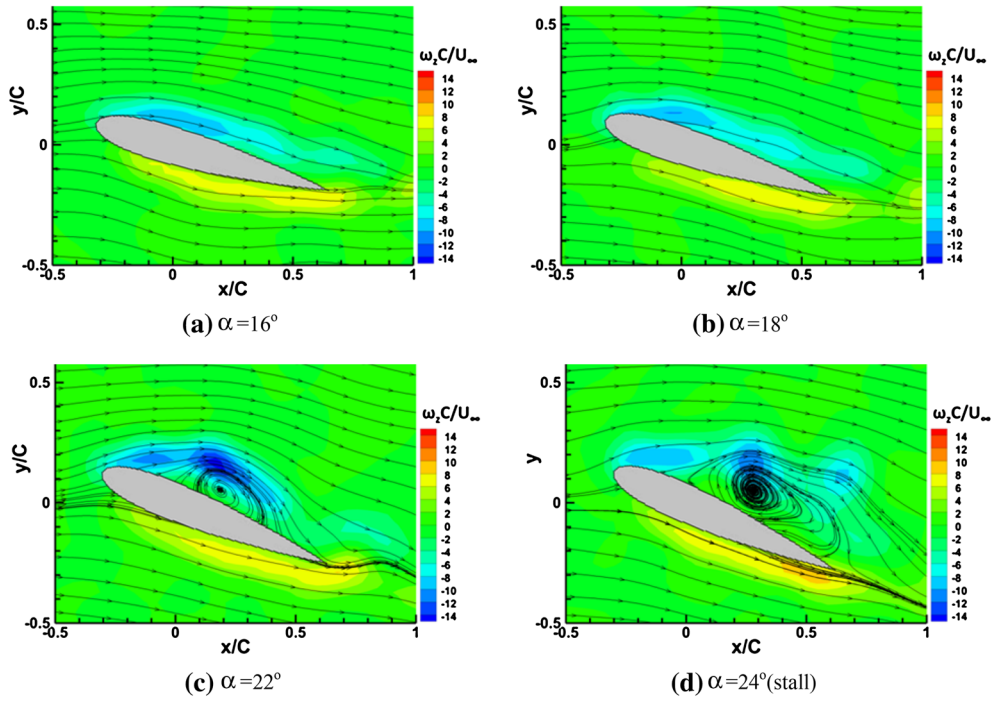
Fig. 8 Instantaneous vorticity field with streamlines at $k = 0.09$ (TI = 6.9 %; $Re = 4.5 \times 10^3$)
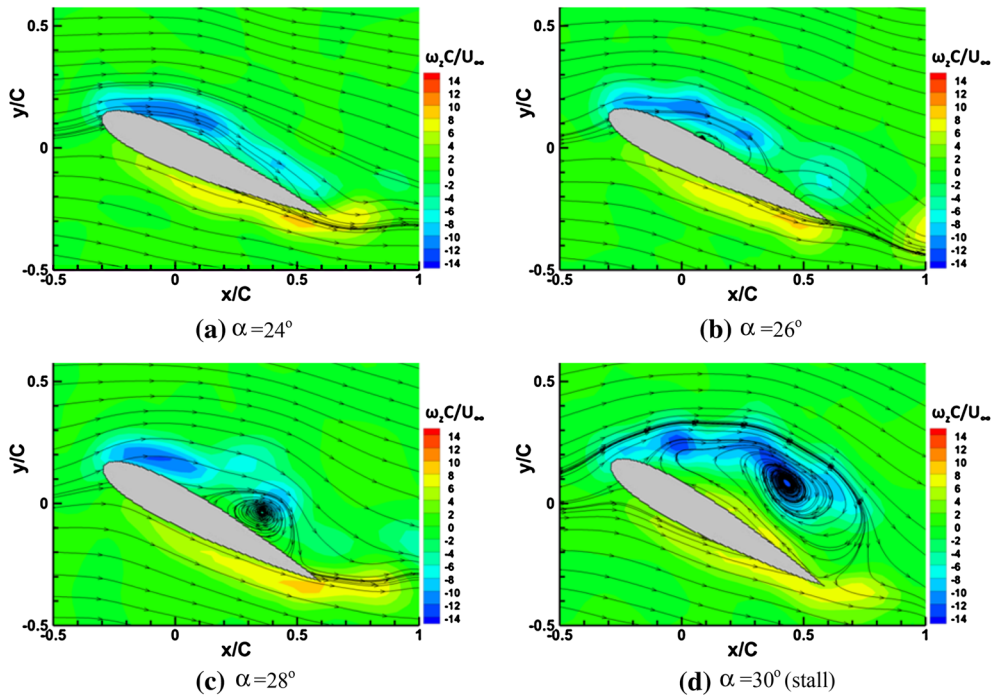

Fig. 9 Instantaneous vorticity field with streamlines at $k = 0.18$ (TI = 6.9 %; $Re = 4.5 \times 10^3$)

The LEV grows in size and becomes an organized dynamic stall vortex from $\alpha = 28°$ to $\alpha = 30°$ in Fig. 9c, d. At $\alpha = 30°$, the organized dynamic stall vortex occupies the whole upper surface. The lift reaches a maximum value as the LEV arrives at the trailing edge.

(a) $\alpha = 24^\circ$

(b) $\alpha = 26^\circ$

(c) $\alpha = 28^\circ$

(d) $\alpha = 30^\circ$

(e) $\alpha = 28^\circ$ (downstroke)

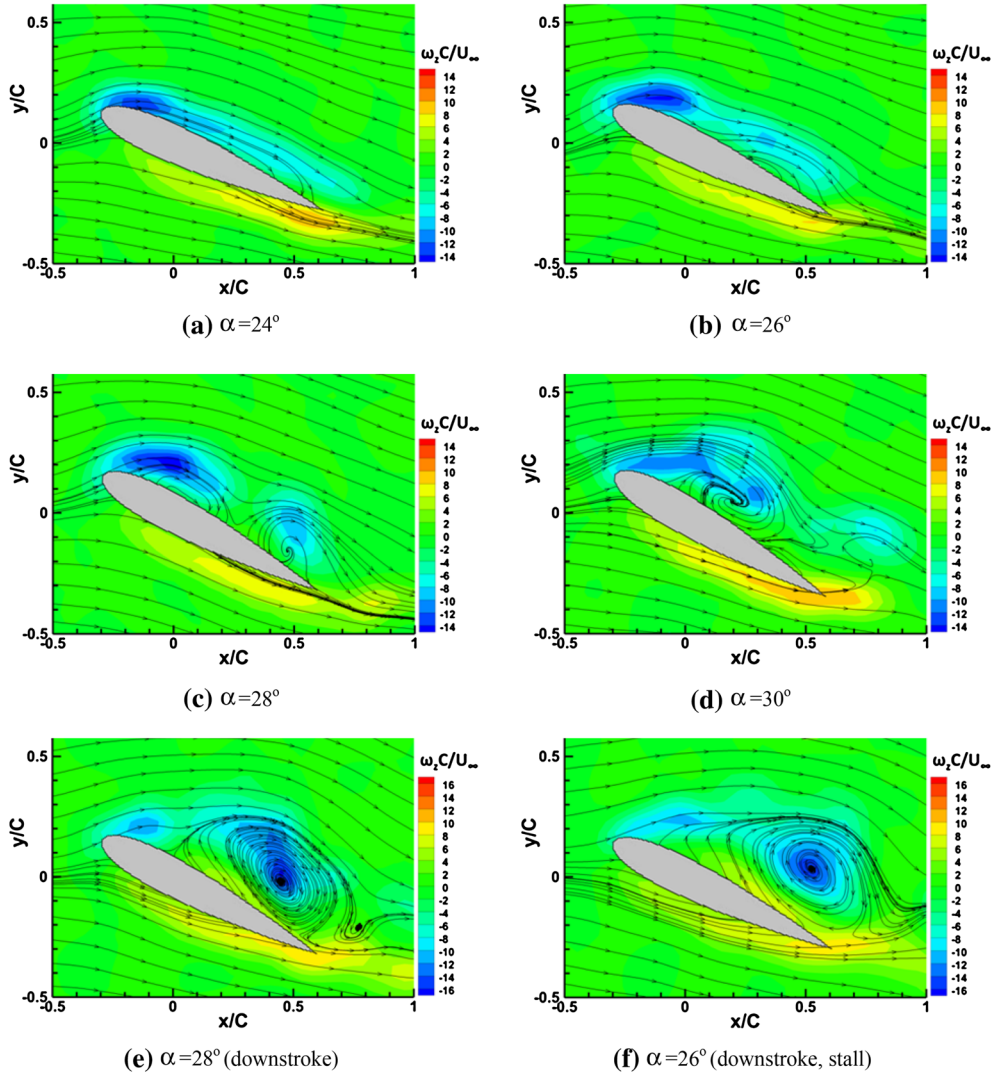**(f)** $\alpha = 26^\circ$ (downstroke, stall)

Fig. 10 Instantaneous vorticity field with streamlines at $k = 0.27$ (TI = 6.9 %; $Re = 4.5 \times 10^3$)

As shown in Fig. 10, when the reduced frequency is increased to $k = 0.27$, the flow evolves slowly and remains attached to the airfoil at $\alpha = 24^\circ$ as shown in Fig. 10a. As the angle of attack pitches up from $\alpha = 26^\circ$ to $\alpha = 30^\circ$ in Fig. 10b–d, the LEV formation takes place and grows on the upper surface. Even though the airfoil pitches up to $\alpha = 30^\circ$, the maximum angle of attack, the LEV still stays on the upper surface of half chord. After pitching motion up to $\alpha = 30^\circ$, the airfoil turns to downstroke. As compared with the flow field at $\alpha = 30^\circ$ between TI = 0.5 % in Fig. 5d and TI = 6.9 % in Fig. 10d, the LEV occupies the whole upper surface and arrives at the trailing edge for the former case, but LEV occupies half chord for the latter. At $\alpha = 28^\circ$ during downstroke as shown in Fig. 10e, the LEV remains above airfoil and moves toward the trailing edge. As the airfoil pitches down to $\alpha = 26^\circ$ as shown in Fig. 10f the LEV arrives at the trailing edge.

In summary, for the freestream with TI = 0.5 %, the stall angles are $\alpha = 16^\circ$, $\alpha = 26^\circ$, and $\alpha = 30^\circ$ for $k = 0.09$, 0.18, and 0.27, respectively. It indicates the stall angles are delayed to high angle with increasing reduced frequency because the oscillation time scale is shorter at higher reduced frequency than lower ones. However, for the freestream with TI = 6.9 %, the stall angles are delayed to $\alpha = 24^\circ$, $\alpha = 30^\circ$, and $\alpha = 26^\circ$ (downstroke) for $k = 0.09$, 0.18, and 0.27, respectively. The delay of stall angle is more pronounced for the freestream with high turbulence intensity. Accordingly, the phase difference of stall angles between TI = 0.5 % and TI = 6.9 % are $\Delta\alpha = 8^\circ$, $\Delta\alpha = 4^\circ$, and $\Delta\alpha = 4^\circ$ for $k = 0.09$, 0.18, and 0.27, respectively. The variation of stall angles is summarized in Table 1.

Table 1 Variation of stall angles with reduced frequency and freestream turbulence intensity

Reduced frequency	TI = 0.5 %	TI = 6.9 %	Phase difference
$K = 0$ (static airfoil)	$\alpha \approx 11°$	N/A	N/A
$K = 0.09$	$\alpha = 16°$	$\alpha = 24$	$\Delta\alpha = 8°$
$K = 0.18$	$\alpha = 26°$	$\alpha = 30$	$\Delta\alpha = 4°$
$K = 0.27$	$\alpha = 30°$	$\alpha = 26$ (downstroke)	$\Delta\alpha = 4°$

The velocity profiles of flow with TI = 0.5 and 6.9 % are compared in Fig. 11 for the stall angles of TI = 0.5 %, $\alpha = 16°$ for $k = 0.09$, $\alpha = 26°$ for $k = 0.18$, and $\alpha = 30°$ for $k = 0.27$. As shown in Fig. 11a, at $\alpha = 16°$, enhanced the turbulence mixing and reduced the velocity deficit ($u/U \leq 1$) which is obvious for TI = 6.9 %. At $\alpha = 26°$ for TI = 6.9 %, as shown in Fig. 11b of the cross section (4), the velocity near the wall surface shows less deficit and recovers to the magnitude of freestream velocity. This is due to the additional momentum transferred from the freestream into the recirculation region. Therefore, instead of the S-shaped velocity profile existed for TI = 0.5 %, the velocity profile is characterized by the boundary layer flow as a result of turbulent mixing along the vertical direction. The similar phenomenon can be seen at $\alpha = 30°$ as shown in Fig. 11c of the cross section (4). The S-shaped velocity profile in the cross section (4) is nearly vanished for TI = 6.9 %. The maximum velocity is reduced from $u/U = 1.8$ to 1.2. The negative velocity (TI = 0.5 %) near the wall surface is nearly absent for TI = 6.9 %. Again, this can be attributed to the enhanced mixing and momentum transfer in the vertical direction. Thus, the dynamic stall is further delayed to the downstroke.

4.3 Circulation

The circulation theory of lift was developed based on inviscid flow. However, this theory is a good approximation for the real viscous flow of typical aerodynamic applications (Digavalli 1994). According to Gharali and Johnson (2013), the LEV is a very low pressure vortex which enriches the strength of circulation resulting in an overshoot in the lift coefficient for pitching airfoils. In this study, circulation was determined using the Stoke's theorem in Eq. (3). The clockwise and counter-clockwise vortices were calculated with a zero threshold value within the unit area.

Figure 12 shows the dimensionless circulation at $k = 0.09$, 0.18, and 0.27. The clockwise vortices are merely considered for the integrated circulation in this study. The x-axis shows that the pitching motion up to $\alpha = 30°$ and then pitching down. Figure 12a shows the integrated circulation value which reaches the maximum around $\alpha = 16°$ with TI = 0.5 % for $k = 0.09$. However, the maximum circulation value occurs at $\alpha = 24°$ with TI = 6.9 %. As the reduced frequency is increased to $k = 0.18$ for TI = 0.5 %, the circulation increases abruptly before the maximum value at $\alpha = 26°$ as shown in Fig. 12b. After $\alpha = 26°$, the circulation drops dramatically. For TI = 6.9 %, the maximum circulation takes place at $\alpha = 30°$ instead. Although both the investigated cases have the similar trend, the phase delay shifts to $\Delta\alpha = 4°$ for the case with TI = 6.9 %. Further increasing the pitching rate up to $k = 0.27$, the maximum circulation value takes place at $\alpha = 30°$, which is the apex of pitching motion, for the case with TI = 0.5 % as shown in Fig. 12c. However, the maximum circulation value postpones to $\alpha = 26°$ during downstroke for the case with 6.9 %.

In summary, the circulation values and thus the lift coefficients increase rapidly to maximum values and drop quickly, especially for $k = 0.18$ and 0.27. This investigation is in good agreement with the results of Prangemeier et al. (2010) and Rival et al. (2010) in terms of the dramatic increase and decrease of circulation values near the stall angle. The growth of LEV which is a coherent structure and the require kinetic energy is supplied by the large velocity gradient from the leading edge. The abrupt drop of circulation values when this kinetic energy connection is cut down and counteraction of TEV (trailing edge vortex) arises. Prangemeier et al. (2010) and Rival et al. (2010) have indicated that the LEV breakdown is associated with massive separations, which then leads to the subsequent rapid decrease in circulation. The angles of maximum circulation values happened are a bit after the dynamic stall which is the angle of LEV reaching the trailing edge of the airfoil.

5 Concluding remarks

The experimental results reported in this paper show that the unsteady flow fields around the NACA 0015 pitching airfoil are investigated by PIV. The specific pitching waveform is used to simulate a vertical axis
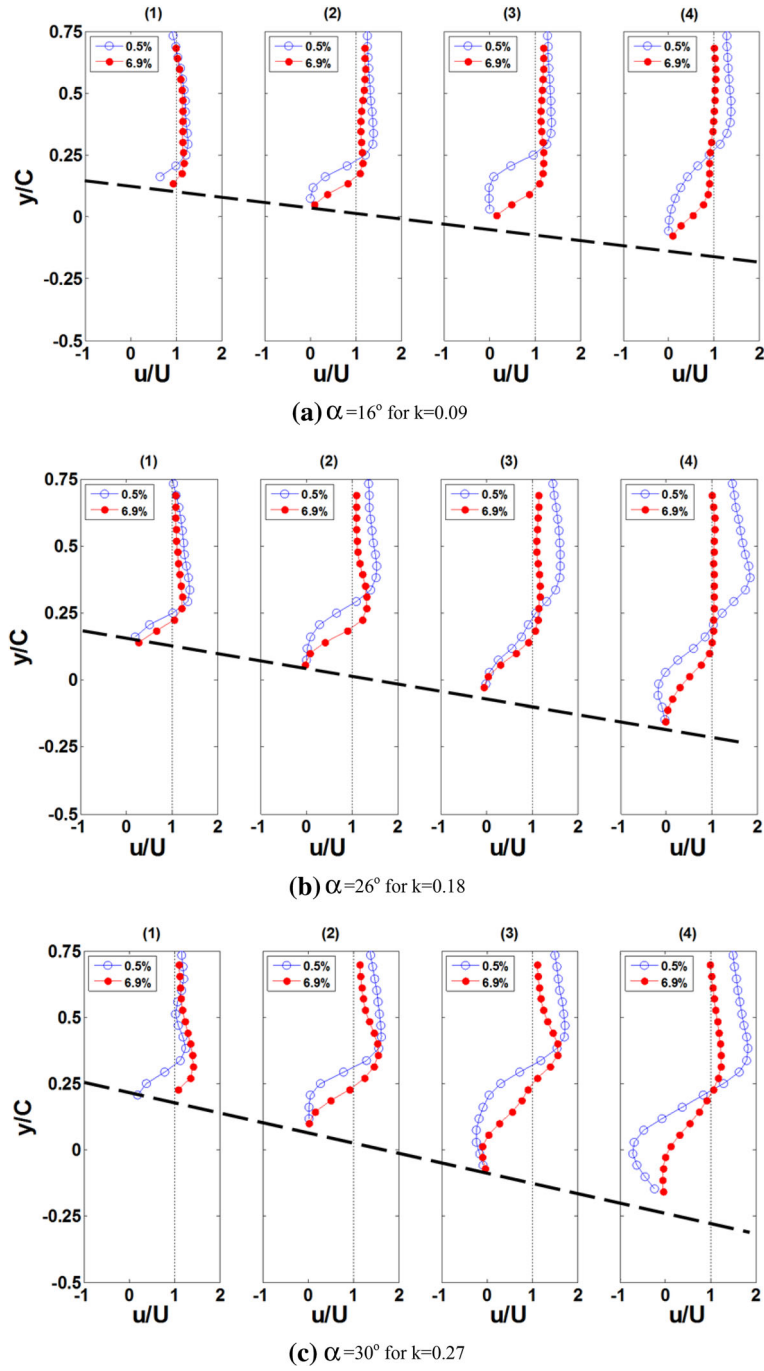
(a) $\alpha = 16°$ for k=0.09

(b) $\alpha = 26°$ for k=0.18

(c) $\alpha = 30°$ for k=0.27

Fig. 11 Comparison of the dimensionless velocity profile (*black dashed line* is wall surface of airfoil)

wind turbine (VAWT) at tip speed ratio $\lambda = 2$. The vorticity contours and streamlines above the upper surface of airfoil have been observed to explore the stall angle. The stall angles for freestream turbulence intensity TI = 0.5 % are $\alpha = 16°$, $\alpha = 26°$, and $\alpha = 30°$ for reduced frequency $k = 0.09$, 0.18, and 0.27, respectively. As found the stall angles of pitching airfoil well in excess the static angle which is $\alpha = 11°$. For TI = 6.9 %, the stall angles are delayed to $\alpha = 24°$, $\alpha = 30°$, and $\alpha = 26°$ (downstroke) for reduced frequency $k = 0.09$, 0.18, and 0.27, respectively. Accordingly, the respective phase difference is $\Delta\alpha = 8°$, $\Delta\alpha = 4°$, and $\Delta\alpha = 4°$. It indicates that the turbulence effect is more pronounced at high reduced frequency.
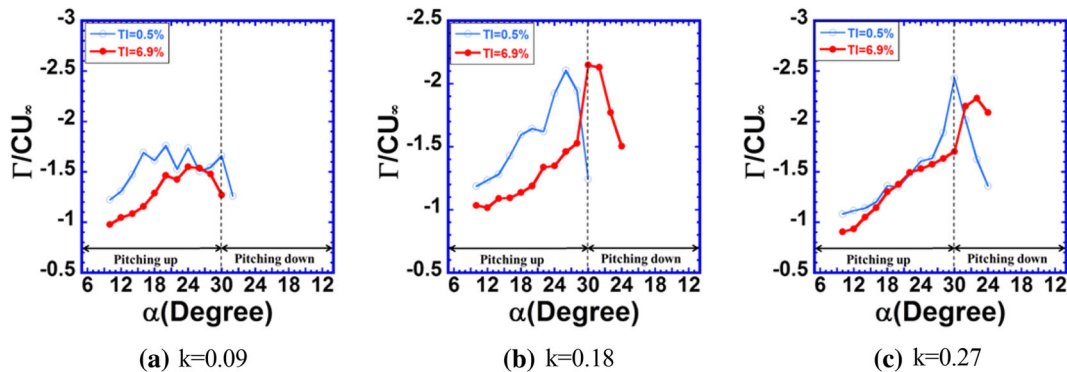
Fig. 12 The dimensionless circulation varies with angle of attack and reduced frequency

For TI = 6.9 %, turbulence mixing is enhanced and the velocity deficit ($u/U \leq 1$) is reduced. The velocity near the wall surface shows less deficit and recovers to the magnitude of freestream velocity at $\alpha = 26°$ for TI = 6.9 %. Therefore, instead of the S-shaped velocity profile existed for TI = 0.5 %, the velocity profile is characterized by the boundary layer flow as a result of turbulence mixing along the vertical direction. The similar phenomenon can be seen at $\alpha = 30°$ for TI = 6.9 %. The S-shaped velocity profile is nearly vanished. The maximum velocity is reduced from $u/U = 1.8$ to 1.2. Thus, the dynamic stall is further delay to the downstroke. In addition, the circulation values increased rapidly before the maximum value reached and dropped quickly for the higher reduced frequency.

References

Ameku K, Nagai BM, Roy JN (2008) Design of a 3 kW wind turbine generator with thin airfoil blades. Exp Thermal Fluid Sci 32:1723–1730. doi:10.1016/j.expthermflusci.2008.06.008

Amet E, Maãžtre T, Pellone C, Achard JL (2009) 2D numerical simulations of blade–vortex interaction in a Darrieus turbine. J Fluids Eng 131:111103. doi:10.1115/1.4000258

Bousman WG (2001) Evaluation of airfoil dynamic stall characteristics for maneuverability. J Am Helicopter Soc 46:239–250

Carr LW (1988) Progress in analysis and prediction of dynamic stall. J Aircr 25:6–17. doi:10.2514/3.45534

Chen C-C, Kuo C-H (2012) Effects of pitch angle and blade camber on flow characteristics and performance of small-size Darrieus VAWT. J Vis 16:65–74. doi:10.1007/s12650-012-0146-x

Chen JS-J, Chen Z, Biswas S, Miau J-J, Hsieh C-H (2010) Torque and power coefficients of a vertical axis wind turbine with optimal pitch control. In: ASME 2010 Power Conference, 2010. American Society of Mechanical Engineers, pp 655–662

Corke TC, Thomas FO (2014) Dynamic stall in pitching airfoils: aerodynamic damping and compressibility effects. Annu Rev Fluid Mech 47:479–505. doi:10.1146/annurev-fluid-010814-013632

Digavalli SK (1994) Dynamic stall of a NACA 0012 airfoil in laminar flow. Ph.D., Massachusetts Institute of Technology

Esfahani JA, Barati E, Karbasian HR (2015) Fluid structures of flapping airfoil with elliptical motion trajectory. Comput Fluids 108:142–155. doi:10.1016/j.compfluid.2014.12.002

Fujisawa N, Takeuchi M (1999) Flow visualization and PIV measurement of flow field around a Darrieus rotor in dynamic stall. J Vis 1:379–386

Gharali K, Johnson DA (2013) Dynamic stall simulation of a pitching airfoil under unsteady freestream velocity. J Fluids Struct 42:228–244. doi:10.1016/j.jfluidstructs.2013.05.005

Gharali K, Johnson DA (2015) Effects of nonuniform incident velocity on a dynamic wind turbine airfoil. Wind Energy 18:237–251. doi:10.1002/we.1694

Hansen KL (2012) Effect of leading edge tubercles on airfoil performance. The Unversity of Adelaide, Adelaide

Islam M, Ting D, Fartaj A (2008) Aerodynamic models for Darrieus-type straight-bladed vertical axis wind turbines. Renew Sustain Energy Rev 12:1087–1109. doi:10.1016/j.rser.2006.10.023

Jin Z, Dong Q, Yang Z (2014) A stereoscopic PIV study of the effect of rime ice on the vortex structures in the wake of a wind turbine. J Wind Eng Indus Aerodyn 134:139–148. doi:10.1016/j.jweia.2014.09.001

Karbasian HR, Esfahani JA, Barati E (2016a) Effect of acceleration on dynamic stall of airfoil in unsteady operating conditions. Wind Energy 19:17–33. doi:10.1002/we.1818

Karbasian HR, Esfahani JA, Barati E (2016b) The power extraction by flapping foil hydrokinetic turbine in swing arm mode. Renew Energy 88:130–142. doi:10.1016/j.renene.2015.11.038

Kurian T, Fransson JHM (2009) Grid-generated turbulence revisited. Fluid Dyn Res 41:021403. doi:10.1088/0169-5983/41/2/021403

Leishman JG (2002) Challenges in modelling the unsteady aerodynamics of wind turbines. Wind Energy 5:85–132

Leishman JG (2006) Principles of helicopter aerodynamics, 2nd edn. Cambridge University Press, New York

McCroskey WJ (1982) Unsteady airfoils. Annu Rev Fluid Mech 14:285–311. doi:10.1146/annurev.fl.14.010182.001441

Miau JJ, Liang SY, Yu RM, Hu CC, Leu TS, Cheng JC, Chen SJ (2012) Design and test of a vertical-axis wind turbine with pitch control. Appl Mech Mater 225:338–343

Prangemeier T, Rival D, Tropea C (2010) The manipulation of trailing-edge vortices for an airfoil in plunging motion. J Fluids Struct 26:193–204. doi:10.1016/j.jfluidstructs.2009.10.003

Rival D, Prangemeier T, Tropea C (2008) The influence of airfoil kinematics on the formation of leading-edge vortices in bio-inspired flight. Exp Fluids 46:823–833. doi:10.1007/s00348-008-0586-1

Rival D, Manejev R, Tropea C (2010) Measurement of parallel blade–vortex interaction at low Reynolds numbers. Exp Fluids 49:89–99. doi:10.1007/s00348-009-0796-1

Taylor G (1935) Statistical theory of turbulence. II. Proc Royal Soc Lond Ser A Math Phys Sci 151:444–454

Tseng C-C, Cheng Y-E (2015) Numerical investigations of the vortex interactions for a flow over a pitching foil at different stages. J Fluids Struct 58:291–318. doi:10.1016/j.jfluidstructs.2015.08.002

Ubaldi M, Zunino P (2000) An experimental study of the unsteady characteristics of the turbulent near wake of a turbine blade. Exp Thermal Fluid Sci 23:23–33

Yen J, Ahmed NA (2013) Enhancing vertical axis wind turbine by dynamic stall control using synthetic jets. J Wind Eng Ind Aerodyn 114:12–17. doi:10.1016/j.jweia.2012.12.015